Experimental assessment of the relationship between rainfall intensity and sinkholes caused by damaged sewer pipes

Tae-Young Kwak[1], Sang-Inn Woo[2], Choong-Ki Chung[3], and Joonyoung Kim[4]

[1]Seismic Safety Research Center, Korea Institute of Civil Engineering and Building Technology, Goyang-si, Gyeonggi-do 10223, South Korea.
[2]Department of Architectural & Civil Engineering, Hannam University, Daedeok-gu, Daejeon 34430, South Korea.
[3]Department of Civil & Environmental Engineering, Seoul National University, Gwanak-gu, Seoul 08826, South Korea.
[4]Division of Smart Interdisciplinary Engineering, Hannam University, Daedeok-gu, Daejeon 34430, South Korea.

Correspondence to: Joonyoung Kim (goldenrain91@gmail.com)

ABSTRACT

In several countries, the rising occurrence of sinkholes has led to severe social and economic damage. Based on the mechanism of sinkhole development, researchers have investigated the correlation between rainfall intensity and sinkholes caused by damaged sewer pipes. In this study, the effect of rainfall intensity on the formation of eroded zones, as well as the occurrence of sinkholes caused by soil erosion due to groundwater infiltration through pipe defects, has been analyzed through model tests. The ground materials in Seoul were represented by weathered granite soil, which is generally used for backfill sewer pipes, and groundwater levels corresponding to three different rainfall intensity conditions were considered. The ground level changes and ground displacements were measured continuously, and the particle image velocimetry (PIV) algorithm was applied to measure the displacement at each position of the model ground. The results indicate that impeding the excessive rise of groundwater levels by securing sufficient sewage treatment facilities can effectively prevent the development of sinkholes caused by pipe defects.

1 Introduction

In recent times, cases of sinkholes have been reported in several countries, such as the US, Japan, Italy, South Africa, China, Spain and South Korea. Major social and economic issues have ensued owing to the resulting structural problems, such as the collapse of buildings and road erosion (Galloway et al., 1999; Waltham et al., 2005; Gutierrez et al., 2008; Kuwano et al., 2010a; Oosthuizen and Richardson, 2011; Beck et al., 2012; Guarino and Nisio, 2012; Yokota et al., 2012; Gao et al., 2013; Intrieri et al., 2015; Bae et al., 2016; Parise, 2019). In general, sinkholes can be classified into two types: (1) natural sinkholes and (2) anthropogenic sinkholes (Guarino and Nisio, 2012; Gutierrez et al., 2008, 2014; Beck, 2012; Parise, 2019). Natural sinkholes occur when the underlying ground layer (e.g., karst landscape) is easily soluble in water, whereas anthropogenic sinkholes may occur also in a non-karst environment (Parise, 2015), caused by human activity such as sewage damage, inadvertent excavation, or groundwater lowering.

Both types of sinkholes have similar mechanisms, and the detailed process of occurrence is as follows (Rogers, 1986; Brinkmann et al., 2008; Caramanna et al., 2008; Kuwano et al., 2010a; Oosthuizen and Richardson, 2011; Martinotti et al., 2017): (1) A cavity is formed underground by external factors (the water-soluble ground layer dissolves in groundwater to cause a natural sinkhole, or soil erosion occurs along with the groundwater outflow due to sewage damage or excavation to cause an anthropogenic sinkhole). (2) The groundwater level rises during rainfall and falls after the rainfall, causing the soil around the cavity to be lost and the cavity to expand. (3) A sinkhole is finally generated because of the repeated increase and decrease of the groundwater level.

Based on the mechanism for both types of sinkholes (natural and anthropogenic), a direct relationship can be inferred between the rainfall intensity, which leads to the transition of the groundwater level (rise and fall), and the occurrence of sinkhole. Notably, the change in climate due to global warming has resulted in higher rainfall intensity with fewer rainy days (Alpert et al., 2002; Kristo et al., 2017; Rahardjo et al., 2019). In South Korea, the maximum daily rainfall has increased over the decades in most regions and is expected to increase significantly in the future (Nadarajah and Choi, 2007; Wi et al., 2016; Choi et al., 2017). For landslides, many studies have established the influences of rainfall on those geological hazards (Peruccacci et al., 2012; Rossi et al., 2012; Vessia et al., 2012). In this context, there is a growing need to study the correlation between rainfall intensity and sinkhole occurrence.

Martinotti et al. (2017) and Parise et al. (2018) showed that a period of torrential rain and the rainfall intensity triggered natural sinkholes in Italy. Gao et al. (2013) confirmed that the groundwater level rise due to extremely heavy rainfall has a significant effect on sinkhole generation in a karst environment in China. Van Den Eeckhaut et al. (2007) showed that the formation of numerous natural sinkholes in Belgium corresponded with periods of high rainfall and high groundwater recharge, which commonly increased the weight of the overburden and decreased its cohesion.

The majority of sinkholes in non-karst environments are known to occur because of damaged sewer pipes. In Seoul, South Korea, an average of 677 sinkholes and subsidence occurred annually from 2010 to 2015, of

which 81.4 % were due to damage to old sewer pipes (Bae et al., 2016). In Japan, local governments in sewage projects were surveyed to identify cases of subsidence due to damage to sewer pipes. As a result, a total of 17,000 data were reported from 2006 to 2009 (Yokota et al., 2012).

Considering these factors, several researchers have conducted statistical analysis and model experiments to investigate the correlation between rainfall intensity and sinkholes caused by damaged sewer pipes. Kwak et al. (2016) showed that the number of anthropogenic sinkhole cases increased with the increase in total monthly precipitation. In addition, it was confirmed that anthropogenic sinkholes are prone to occur after exceptionally heavy rains. By quantifying Pearson's correlation coefficient between two relevant observations, Choi et al. (2017) showed that the monthly accumulated precipitation and the quantity of subsidence are related to a certain extent. Guo et al. (2013) and Tang et al. (2017) used model experiments and evaluated the effect of the defect size, groundwater level, and particle size on soil erosion due to groundwater infiltration through pipe defects. However, they only used non-cohesive soils and covered extreme cases with groundwater levels significantly exceeding the ground level.

In this study, the urban area in Seoul has been simulated, and model tests have been conducted to analyze the effect of rainfall intensity on the formation of eroded zones, as well as the occurrence of sinkholes caused by soil erosion due to groundwater infiltration through pipe defects. The model ground was constructed using weathered granite soil (which is generally cohesive), mainly used to backfill the sewer pipes in Seoul. Three rainfall intensity conditions (heavy rainfall, very heavy rainfall, and extremely heavy rainfall) were set for the groundwater level, based on summer rainfall patterns in Korea, to be applied in the model tests. The groundwater level change, discharged soil volume, and ground displacement were measured continuously throughout the tests. In particular, the particle image velocimetry (PIV) method, which can continuously measure and analyze the displacements in the ground, was applied to quantify the ground deformation with the occurrence and expansion of underground cavities.

The remainder of this paper is organized as follows. Section 2 describes the model test device, model grounds, and test conditions. Section 3 discusses the model test results. Finally, Section 4 presents the conclusions.

2 Experimental program

2.1 Experiment apparatus

In this study, experiments were performed using the model tester developed by Kwak et al. (2019) to simulate ground subsidence (Figure 1). The distance between each pipe in the sewer pipe network in Seoul was examined and found to be around 1.2 m. In order to exclude the effects of unnecessary boundary conditions, the width of the model soil was set to 1.4 m, with respective left and right margins of 0.1 m. Considering that the average landfill depth of a sewage pipe in Seoul is 0.9 m (Kim et al., 2018), the soil chamber was built to a height of 1.0 m, including a 0.1 m clearance to facilitate sample composition. The depth of the soil chamber

96   was set to 0.1 m to simulate the plane strain condition, and the front plate of the chamber was made of acrylic

97   plate to allow the inside of the ground to be photographed during the test.

98   A slit was installed at the bottom of the soil chamber to simulate the damage of the sewer pipe allowing the

99   inflow and outflow of sewage and the outflow of soil during the model test. The width of the slit(B) was set

100   to 2 cm, based on the study by Mukunoki et al. (2012), such that B/D_{max} was 4.2 (maximum particle diameter

101   of weathered soil D_{max} = 4.76 mm). A supply valve and a drain valve were installed under the slit to control

102   the inflow and outflow of groundwater as well as the outflow of eroded soil. The external water tank

103   connected to the inlet valve was designed to maintain a constant level even when water is continuously

104   supplied to the model ground. Through experimental assessment (Table 1), the National Diaster Management

105   Institute of Korea (2014) suggested a relationship between the rainfall intensity and the hydraulic head in the

106   sewage network conditions near Gangnam station (sewer pipe with 1000 mm of diameter was simulated). It

107   should be noted that the hydraulic head increases linearly with the rainfall strength until the rainfall strength

108   is 40 mm/h, but thereafter increases sharply. In the present study, the height of the external tank was made

109   adjustable to simulate the various rainfall intensity (related to hydraulic head).

110   **2.2 Model ground**

111   The vast majority of prior studies that have experimentally assessed the ground subsidence and sinkhole due

112   to sewer pipe damage have been conducted on poorly-graded non-cohesive soils (Kuwano et al., 2010a,

113   2010b; Guo et al., 2013; Sato and Kuwano, 2015; Indiketiya et al., 2017; Tang et al., 2017). However, in

114   several countries, the sewage reclamation specifications allow the landfill soil to contain 15–25 % of fine

115   contents. There are no restrictions on particle size distribution apart from the maximum particle size (Japan

116   Road Association, 1990; Ministry of Environment of Korea, 2010). In the present study, to simulate the

117   ground in Seoul in which weathered granite soil, which is a well-graded cohesive soil, is widely distributed,

118   the model ground was created by collecting Gwanak weathered soil and adjusting the fine content to 7.5% to

119   meet the fine content standard. The degree of compaction was also set to 93 % of the standard maximum unit

120   dry weight $\gamma_{d,max}$ to satisfy the sewer pipe landfill standards, and the model ground was constructed with the

121   optimum moisture content. Figure 2 shows the particle size distributions of the adjusted and natural Gwanak

122   soil in comparison with the sewer pipe landfill standards in South Korea and Japan. Table 2 lists the basic

123   physical properties, strength parameters and saturated permeability coefficient of the adjusted Gwanak soil

124   used in the model test.

125   **2.3 Digital image analysis**

126   In geotechnical engineering, digital imaging techniques are primarily used to measure the deformation of

127   target samples (Alshibli and Sture, 1999; White et al., 2003; Indiketiya et al., 2017; Kim et al., 2017; Kwak

128   et al., 2019). In the present study, the displacement at each position of the model ground was measured by

129   applying the PIV algorithm (Adrian, 1991), which is the most widely used technique in the field of

geotechnical engineering. The PIV cross-correlation on the pixel sets of the pre-deformation and post-deformation images were calculated to obtain the point with the highest correlation. The position of the sample set with the highest correlation is used to estimate the relative displacement at each position of the sample (Kim et al., 2011; White et al., 2003). In this study, the internal displacement of the sample was evaluated using GeoPIV (White and Take, 2002), a commercial program that is widely used to apply the PIV technique in geotechnical engineering. With the displacement, the volume and shear strain are estimated together for the analysis.

In general, when applying the PIV technique, high accuracy analysis results can be obtained when the uniqueness of the pixel set increases with the size of the pixel set. However, in order to calculate displacements at various positions, it is necessary to set an appropriate size for the set of pixels. Accuracy and precision verification of the GeoPIV program was performed for various-sized pixel subsets (40x40, 60x60, 80x80, 100x100, and 120x120) by comparing two digital images: the original image of the model ground and the image artificially shifted by ten pixels at the four edges of the model ground. The optimum size of the pixel set was chosen as 100 by 100 pixels, which shows a 0.0069 pixel maximum error in accuracy and precision. As shown in Figure 3, the PIV technique was applied to the positions of a total of 2600 pixel subsets (65 by 40). To minimize the boundary effect between the interface of the sample and the soil chamber, the vicinity of the wall was excluded from the analysis. In addition, any excessive relative displacement due to soil erosion (no highly correlated pixel sets found in the post-deformation image) was excluded from the analysis.

2.4 Test procedures

Once the model ground was created, the model tests which consisted of a water supply stage and a water drainage stage were conducted. The water supply stage represents the infiltration of sewer water from the pipes to the ground through damaged sections during heavy rainfall periods. This phenomenon was simulated in the model test by introducing water from the external water tank into the soil chamber through the supply valve and slit to reach the target groundwater level (i.e. hydraulic head). After heavy rainfall, the hydraulic pressure of a sewer pipe becomes lower (as the sewer pipe becomes vacant), thus, it is the most likely that the groundwater will flow back through the damaged section. The water drainage stage simulates the drainage of groundwater into the sewer pipes through the damaged sections after heavy rainfall periods by closing the supply valve and opening the drainage valve. The soil also discharged through the lower slit along with the water drainage. Table 3 shows the conditions of the three model tests conducted in this study, simulating cases with rainfall intensities of 40 mm/h (represent the rainfall intensity of heavy rain watch in South Korea) and 50 mm/h (represent the rainfall intensity of heavy rain warning in South Korea) presented in Table 1, as well as that with the groundwater level rising to the ground surface.

Linear variable displacement transducers (LVDTs) were installed at three locations on the surface of the ground, at 0, 30, and 60 cm from the center of the soil chamber, to measure the surface displacement during

165 the tests (Figure 1). During the model tests, digital images of the ground were continuously captured, and the

166 PIV technique was applied to analyze the displacement and deformation (Adrian, 1991; Alshibli and Akbas,

167 2007; Kim et al., 2017; Kwak et al., 2019). In addition, the amount of soil discharged through the slit was

168 measured after the water supply and water drainage stages of each test.

169 **3 Experimental results and discussion**

170 **3.1 Test 1: Heavy rainfall intensity (47 cm hydraulic head)**

171 **3.1.1 Water supply stage**

172 Test 1 was conducted by introducing groundwater to a 47 cm initial hydraulic head (the height difference

173 between the slit and weir in the water tank) to simulate a heavy rainfall intensity of 40 mm/h. In the water

174 supply stage of Test 1, no soil deformation occurred on the ground surface (measured by the LVDTs) and in

175 the ground (measured by the PIV technique) as the groundwater level approached 47 cm. Immediately after

176 opening the slit, the water pressure acting on the ground directly above the slit was 4.5 kPa, and the vertical

177 earth pressure generated by the upper soil was about 16.7 kPa. Therefore, under this condition, the soil always

178 had a positive effective stress, and the piping phenomenon did not occur. In this study, since the model ground

179 was densely constructed (D_R = 78 %) with a sufficient degree of compaction (R_C = 93 %) according to

180 domestic specification, no water compaction (Kwak et al., 2019), which occurs mainly when sewage flows

181 into a loose sandy soil, was observed. From these results, it was confirmed in this experimental case that the

182 resistance factor (due to the soil strength parameter) was greater than the sum of the drag force (upward force

183 by infiltration pressure during water supply) and the gravity (downward force).

184 **3.1.2 Water drainage stage**

185 In the water drainage stage of Test 1, no soil deformation was observed on the ground surface as in the water

186 supply stage. The deformation in the ground was evaluated by applying PIV to the images captured during

187 the test. Figures 4, 5, 6 are the PIV analysis results showing the estimated displacement vector, volume, and

188 shear strain increments in six phases: (a) 0–30 s, (b) 30–60 s, (c) 60–90 s, (d) 90–120 s, (e) 120–150 s, and

189 (f) 150–180 s. For the volumetric strain, the red grid (the area with positive values) indicates that the area has

190 expanded, and the blue grid (the area with negative values) indicates that the area has been compressed.

191 In the water drainage stage, the water pressure applied through the slit disappeared, and the groundwater in

192 the soil chamber was discharged quickly through the slit. Unlike in the water supply stage, the ground below

193 the groundwater level became saturated and lost its apparent cohesion. The rapid outflow of groundwater

194 resulted in a downward infiltration into the ground, and the soil was discharged from the area immediately

195 above the slit, where there was no active restraining pressure (and thus, no shear strength), along with the

196 groundwater.

197 During the initial phase of the water drainage stage (0–60 s), the soil was discharged through the slit, causing
198 a downward displacement in the periphery of the cavity, and a triangular cavity was formed just above the
199 slit (Figure 4a and b). In addition, volume and shear strain increments occurred intensively around the cavity
200 (Figure 5a, b, Figure 6a and b). In the 60–90 s interval of the water drainage stage, as shown in Figure 4c,
201 the soils on both sides of the cavity collapsed, and the cavity expanded laterally. The volume and shear strain
202 increments were concentrated in small areas near the cavity, similar to the initial stage (Figure 5c and Figure
203 6c).
204 As shown in Figure 4d, during the 90–120 s interval of the groundwater drainage stage, the lateral expansion
205 of the cavity inside the ground was completed, and no downward displacement was observed in the upper
206 part of the cavity and the soils on the sides. The volume and shear strain increments were also not observed
207 in the outer region of the cavity (Figure 5d and Figure 6d). In this phase, the cavity collapsed; the soil
208 accumulated near the slit gradually shifted to escape into the slit, and the deformation was concentrated near
209 the slit. After 120 s, the soil regained its apparent adhesion due to surface tension, and its outflow stabilized
210 as the drainage completed. Finally, a mushroom-shaped cavity was formed (Figure 4e and f).

211 **3.2 Test 2: Very heavy rainfall intensity (70 cm hydraulic head)**

212 **3.2.1 Water supply stage**

213 Test 2 was conducted by setting the maximum groundwater level to 70 cm to simulate a high rainfall intensity
214 of 50 mm/h. During the water supply stage of Test 2, no soil deformation was observed on the ground surface
215 and in the ground by both LVDT and PIV analyses. As a result, owing to the soil strength parameter, the
216 resistance factor was found to remain greater than the sum of the drag force (upward force by infiltration
217 pressure during water supply) and the gravity (downward force), despite the application of a higher hydraulic
218 pressure in Test 2 as compared to that in Test 1.

219 **3.2.2 Water drainage stage**

220 During the water drainage stage of Test 2, no vertical displacement was observed on the surface of the model
221 ground. The displacement of the soil element according to the development of the underground cavity was
222 observed by the PIV technique. Figures 7, 8, and 9 show the displacement increment vectors, incremental
223 volumetric strain distribution, and incremental shear strain distribution, respectively; the analysis was
224 conducted in four phases: 0–30 s, (b) 30–60 s, (c) 60–90 s, and (d) 90–120 s (the displacement ended within
225 120 s).
226 In the initial phase of the water drainage stage (0–30 s), the soil was discharged through the slit, causing an
227 internal collapse near the slit. Thus, an underground cavity was formed (Figure 7a), differing from that in
228 Test 1 in terms of shape as well as location; it was located close to the maximum groundwater level (about
229 60 cm from the bottom plate). These results indicate that the hydraulic pressure (related to rainfall intensity)
230 affects the shape and location of the underground cavity in the water drainage stage. In Test 1, the eroded

231 zone was formed up to about 89 % of the maximum groundwater level. In Test 2, it developed up to about

232 86 %. When a poorly-graded non-cohesive soil was used under the same experimental conditions, the cavity

233 developed up to 107 % of the maximum groundwater level (Kwak et al., 2019). This shows that the well-

234 graded cohesive soil used in this study has a greater resistance to soil erosion. In addition, during the initial

235 stage (0–30 s), the incremental volumetric and shear strains were found to be concentrated in the upper area

236 of the underground cavity (Figure 8a and Figure 9a).

237 During the 30–90 s phase, downward displacement was no longer observed at the top of the cavity;

238 displacement in the slit direction occurred only in the left and right areas adjacent to the cavity (Figure 7b

239 and c). The volumetric and shear strains also showed a tendency to be concentrated in the left and right areas

240 where the displacement occurred, indicating that the cavity gradually increased laterally (Figure 8b, c, Figure

241 9b, and c). In the process of forming a cavity, the downward infiltration pressure was low, and the soil that

242 had lost strength accumulated near the slit. On the other hand, when the downward infiltration pressure was

243 higher, all the soil that had lost strength escaped, resulting in the formation of an oval cavity. After 90 s, as

244 the groundwater level was exhausted, the unsaturated strength of the ground was restored, and no further

245 displacement or deformation were observed inside the ground (Figure 7d, Figure 8d, and Figure 9d).

246 **3.3 Test 3: Extremely heavy rainfall intensity (90 cm hydraulic head)**

247 **3.3.1 Water supply stage**

248 Test 3 was conducted to simulate the intensity of an extremely heavy rainfall that causes the groundwater

249 level to rise up to the surface of the ground. In the water supply stage of Test 3, significant displacements

250 were measured on the surface (LVDTs) and inside the model ground (PIV). Figure 10 shows the surface

251 displacement over time, with a gradual subsidence after approximately 2400 s. The ground displacements

252 identified by the PIV technique from 0–2000 s also showed no specific behaviors. Therefore, the internal

253 displacement vectors identified as a result of the PIV technique after 2000 s are shown in Figure 11, overlaid

254 onto the final photograph of each step: (a) 2000–2400 s, (b) 2400–2800 s, (c) 2800–3200 s, and (d) 3200–

255 3600 s.

256 As the groundwater level reached about 75 cm (83 % of ground height), soil particle displacement was

257 observed in the soil from 2000–2400 s. This result indicates that, owing to the strength of the soil, the

258 resistance factor becomes smaller as the model ground is saturated, and the weight of the soil in the saturated

259 region cannot be supported. Since the soil in the upper part of the groundwater level still maintained its

260 unsaturated strength, the downward displacement appeared only in the area adjacent to the groundwater level.

261 There was still no subsidence observed on the surface (Figure 11a).

262 From 2400–2800 s, downward displacement towards the slit was observed throughout the soil area. In

263 particular, a larger downward displacement was observed in the inverted triangle region above the slit, which

264 was significantly affected by the inflow of groundwater (Figure 11b). As the groundwater level rose, the

265 matric suction expressed in the unsaturated region of the ground decreased. Therefore, the subsidence on the

266 ground surface was also measured from this phase. From 2800–3200 s, the groundwater level reached 80 cm

267 from the bottom (89 % of ground height), and the maximum downward displacement of the entire water

268 supply stage was observed during this phase (Figure 11c). This indicates that infiltration occurs when the

269 groundwater level approaches the ground surface, and the soil structure is no longer supported as there is no

270 longer sufficient matric suction in the ground directly above the groundwater level. After 3200 s, downward

271 displacement occurred continuously throughout the soil area until groundwater level reaches the target level

272 (Figure 11d).

3.3.2 Water drainage stage

274 The water drainage stage of Test 3 was divided into four phases for the analysis: (a) 0–30 s, (b) 30–60 s, (c)

275 60–90 s, and (d) 90–120 s. The displacement increment vectors, incremental volumetric strain distributions,

276 and incremental shear strain distributions of each stage are shown in Figures 12, 13 and 14, respectively,

277 overlaid onto the photograph of the target ground taken at the end of each phase.

278 In the initial phase (0–30 s) of the water drainage stage of Test 3, the groundwater was rapidly discharged

279 into the slit owing to high downward infiltration pressure. As the soil particles escaped along with the

280 groundwater discharge, the upper ground collapsed, forming an anthropogenic sinkhole similar in shape to

281 the punching shear failure (Figure 12a). In the previous tests, the cavities formed up to about 86 % and 89 %

282 of the maximum groundwater level. The shape of the formed anthropogenic sinkhole indicated significant

283 downward displacement (of the soil that had lost strength) towards the slit. The sudden collapse of the ground

284 clogged the slit, which in turn prevented soil discharge. At this time, the shear deformation also showed a

285 tendency to be concentrated around the collapsed soil (Figure 14a). After the soil was completely drained,

286 no significant deformation inside the ground and on the ground surface were observed via the PIV technique

287 and the LVDTs after 30 s, as the matric suction allowed the ground to recover its unsaturated strength.

3.4 Comparative Study

289 To quantitatively analyze the effect of rainfall intensity on ground cavity and sinkhole development, the

290 evolution of the cavity size with time in the water drainage stage was obtained for each test, and the time at

291 which the water was completely drained was also displayed, as shown in Figure 15. For the hydraulic pressure

292 of 45 cm and 70 cm, the time taken for the groundwater to drain completely was 70 s and 90 s, respectively.

293 However, in Test 3, although the groundwater level was higher, the soil collapsed instantly, resulting in an

294 anthropogenic sinkhole, and the time taken for complete drainage was 80 s, which was faster than that in Test

295 2. After the drainage was completed, the cavity sizes measured in Test 1 and Test 2 were 497 cm^2 (66 % of

296 the final cavity size of 742 cm^2) and 1286 cm^2 (87 % of the final cavity size of 1482 cm^2), respectively. In

297 both Tests 1 and 2, the cavity expanded for about 30 s after the drainage was completed, at which time its

298 size tended to stabilize. In Test 3, where the anthropogenic sinkhole occurred, a cavity of 1207 cm^2 (56 % of

299 the final cavity size of 2171 cm^2) was formed after the drainage was completed, after which the cavity

300 continued to expand for approximately 200 s.

301 Table 4 shows the ratio of the weight of the total soil volume to the weight of the discharged soil volume, the

302 volume ratio of the area corresponding to the cavity, and the weight ratio of the loosening zone, respectively.

303 The size and internal density change of the loosening zone were calculated by the following method. (1)

304 After completion of the test, the discharged soil was dried to measure the weight. (2) The weight of the area

305 corresponding to the cavity was calculated by multiplying the calculated volume of the cavity by the initial

306 density of the soil. The soil weight corresponding to the loosening zone was calculated through the difference

307 between the results of steps (1) and (2). (3) The size of the loosening zone was calculated by excluding the

308 area corresponding to the cavity from the area overlapping with the volumetric strain calculated in each step.

309 (4) The internal density change was confirmed using the results of steps (2) and (3).

310 As shown in Table 4, the size and density change of the loosening area were found to be nearly identical in

311 the three tests. On the other hand, as the hydraulic head increased, the weight and volume of the eroded zone

312 and the average width of the cavity relative to the slit width increased linearly. However, recalling the fact

313 that the hydraulic head increased drastically when the rainfall intensity exceeds a certain threshold, it can be

314 inferred that the volume of the discharged soil and the size of the eroded zone may also increase exponentially

315 with rainfall intensity. The threshold value is definitely specific to a given sewer-system. Thus the

316 experimental results of this study suggest that to prevent sinkholes caused by pipe defects, sewage pipe

317 network facilities need to be expanded to inhibit the rapid rise of groundwater levels in preparation for

318 increased torrential rain caused by climate change.

319 **4 Conclusions**

320 In this study, model tests were used to analyze the effects of rainfall intensity on the formation of the eroded

321 zone and the occurrence of sinkholes caused by soil erosions due to groundwater infiltration through pipe

322 defects. The model tests were conducted to simulate the actual site conditions as far as possible by using the

323 soil used around sewer pipe networks and the sewer pipe landfill standards as well as a large-scale soil

324 chamber. The groundwater level was applied to the model tests by setting three hydraulic heads based on the

325 heavy rainfall characteristics of South Korea: (1) heavy rainfall intensity (47 cm hydraulic head); (2) very

326 heavy rainfall intensity (70 cm hydraulic head); and (3) extremely heavy rainfall intensity (90 cm hydraulic

327 head). Throughout the model tests, the groundwater level changes and the ground surface displacements were

328 measured continuously from the start to the end of the tests. In addition, the PIV technique, which can

329 continuously measure and analyze the displacement of the entire ground, was applied to quantify the ground

330 deformation (volumetric strain and shear strain), generation, and expansion of the underground cavity. Based

331 on the results of the three tests, the following observations were drawn:

332 (1) The rainfall intensity considerably affected on the ground deformation during and after a rainfall.

333   (2) Under heavy and very heavy rainfall intensity conditions, no internal soil deformation occurred while the

334   groundwater level was rising. However, under extremely heavy rainfall intensity conditions, ground

335   subsidence was observed. This result indicates that the resistance factor (due to the soil strength parameter)

336   becomes smaller than the sum of the drag force (upward force by infiltration pressure during water supply)

337   and the gravity (downward force) when the rainfall intensity exceeds a certain threshold, which was found

338   to have a hydraulic head between 70 cm and 90 cm under the given system.

339   (3) After heavy rainfall (that leads to the rise of the groundwater level due to the infiltration of groundwater

340   through the sewer pipe defects), the soil was discharged from the area above the slit with the rapid outflow

341   of groundwater, where there was no active restraining pressure. During the formation and development of

342   cavity along with the drop in the groundwater level, the incremental volumetric and shear strains were

343   concentrated in the vicinity of the underground cavity.

344   (4) The height and average width of cavities increased linearly with the applied hydraulic head, and notably,

345   sinkhole opened under extremely heavy rainfall intensity. Referring the previous study which showed the

346   relationship between the hydraulic head and rainfall intensity, the discharged soil and the size of the eroded

347   zone may increase exponentially with rainfall intensity.

348   It should be noted that the hydraulic head-rainfall intensity relationship used in this study is site-specific. The

349   induced hydraulic head under the same rainfall intensity can be different site to site. Nevertheless, the

350   experimental observations of this study confirm the influence of rainfall intensity on the soil erosion near the

351   sewer pipe defects as well as sinkhole occurrence and suggest a necessity of sewage pipe network facilities

352   rehabilitation in preparation for increased torrential rain caused by climate change.

353   **Data availability**

354   Data from this research are not publicly available. Interested researchers can contact the corresponding author

355   of this article.

356   **Author contribution**

357   The conceptualization was done by TYK, CKC, and JK planned methodology. TYK performed the analysis

358   using software, and validation was performed by SIW and CKC. JK performed formal analysis. TYK

359   prepared the original draft, while all authors contributed to the review and editing. Visualization and graphics

360   were designed by TYK and JK. SIW and CKC supervised the research work.

361   **Competing interests**

362   The authors declare that they have no conflict of interest

363 **Acknowledgements**

364 This research was supported by the Research Institute at the college of Engineering of Seoul National

365 University. In addition, the support of Jin-Tae Han, research fellow of the Korea Institute of Civil Engineering

366 & Building Technology, is greatly appreciated.

367 **Financial support**

368 This research was supported by a grant (code: 20SCIP-C151438-02) from Construction Technologies

369 Program funded by Ministry of Land, Infrastructure and Transport of Korean government. Also, this work

370 was supported by the National Research Foundation of Korea (NRF) grant funded by the South Korean

371 government (MSIP) (No. 2015R1A2A1A01007980).

372 **References**

373 Adrian, R. J.: Particle-Imaging Techniques for Experimental Fluid Mechanics, Annu. Rev. Fluid Mech.,

374 23(1), 261–304, doi:10.1146/annurev.fl.23.010191.001401, 1991.

375 Alpert, P., Ben-Gai, T., Baharad, A., Benjamini, Y., Yekutieli, D., Colacino, M., Diodato, L., Ramis, C.,

376 Homar, V., Romero, R., Michaelides, S. and Manes, A.: The paradoxical increase of Mediterranean

377 extreme daily rainfall in spite of decrease in total values, Geophys. Res. Lett., 29(11), 29–32,

378 doi:10.1029/2001GL013554, 2002.

379 Alshibli, K. A. and Akbas, I. S.: Strain Localization in Clay: Plane Strain versus Triaxial Loading

380 Conditions, Geotech. Geol. Eng., 25(1), 45–55, doi:10.1007/s10706-006-0005-4, 2007.

381 Alshibli, K. A. and Sture, S.: Sand Shear Band Thickness Measurements by Digital Imaging Techniques, J.

382 Comput. Civ. Eng., 13(April), 103–109, doi:10.1061/(ASCE)0887-3801(1999)13:2(103), 1999.

383 Bae, Y., Shin, S., Won, J. and Lee, D.: The Road Subsidence Conditions and Safety Improvment Plans in

384 Seoul, Seoul., 2016.

385 Beck, B.: Soil Piping and Sinkhole Failures. In: Encyclopedia of Caves (Second Edition), White, W. B. and

386 Culver, D. C. (Eds.), Academic Press, Amsterdam, 2012.

387 Brinkmann, R., Parise, M. and Dye, D.: Sinkhole distribution in a rapidly developing urban environment:

388 Hillsborough County, Tampa Bay area, Florida, Eng. Geol., 99(3–4), 169–184,

389 doi:10.1016/j.enggeo.2007.11.020, 2008.

390 Caramanna, G., Ciotoli, G. and Nisio, S.: A Review of Natural Sinkhole Phenomena in Italian Plain Areas,

391 Nat. Hazards, 45(2), 145–172, doi:10.1007/s11069-007-9165-7, 2008.

392 Choi, C., Kim, J., Kang, J. and Park, Y.: Ground Subsidence Risk Analysis with Intensity and Duration of

393 Rainfall, Mod. Environ. Sci. Eng., 3(03), 162–167, doi:10.15341/mese(2333-2581)/03.03.2017/003, 2017.

394 Galloway, D., Jones, D. R. and Ingebritsen, S. E.: Land Subsidence in the United States, United States

395 Geol. Surv. Circ. 1182, 177, 1999.

396 Gao, Y., Luo, W., Jiang, X., Lei, M. and Dai, J.: Investigations of Large Scale Sinkhole Collapses, Laibin,

397 Guangxi, China, in National Cave and Karst Research Institute Symposium 2, pp. 327–331, Carlsbad, New

398 Mexico., 2013.

399 Guarino, P. M. and Nisio, S.: Anthropogenic Sinkholes in the Territory of the City of Naples (Southern

400 Italy), Phys. Chem. Earth, 49, 92–102, doi:10.1016/j.pce.2011.10.023, 2012.

401 Guo, S., Shao, Y., Zhang, T., Zhu, D. Z., Asce, M. and Zhang, Y.: Physical Modeling on Sand Erosion

402 around Defective Sewer Pipes under the Influence of Groundwater, Journal of Hydrualic Engineering,

403 139(December), 1247–1257, doi:10.1061/(ASCE)HY.1943-7900.0000785., 2013.

404 Gutiérrez, F., Guerrero, J. and Lucha, P.: A genetic classification of sinkholes illustrated from evaporite

405 paleokarst exposures in Spain. Environ. Geol. 53, 993–1006, doi: 10.1007/s00254-007-0727-5, 2008.

406 Gutierrez, F., Parise, M., De Waele, J. and Jourde, H.: A review on natural and human-induced geohazards

407 and impacts in karst. Earth Science Reviews, 138, 61-88, doi: 10.1016/j.earscirev.2014.08.002, 2014.

408 Indiketiya, S., Jegatheesan, P. and Pathmanathan, R.: Evaluation of Defective Sewer Pipe Induced Internal

409 Erosion and Associated Ground Deformation Using Laboratory Model Test, Can. Geotech. J., 54(8), 1184–

410 1195, doi:https://doi.org/10.1139/cgj-2016-0558, 2017.

411 Intrieri, E., Gigli, G., Nocentini, M., Lombardi, L., Mugnai, F., Fidolini, F. and Casagli, N.: Sinkhole

412 monitoring and early warning: An experimental and successful GB-InSAR application, Geomorphology,

413 241, 304–314, doi:10.1016/j.geomorph.2015.04.018, 2015.

414 Japan Road Association: Earth works manual, 1990.

415 Kim, J., Jang, E.-R. and Chung, C.-K.: Evaluation of Accuracy and Optimization of Digital Image Analysis

416 Technique for Measuring Deformation of Soils, J. Korean Geotech. Soc., 27(7), 5–16, 2011.

417 Kim, J., Woo, S. I. and Chung, C.: Assessment of Non-uniform Deformation during Consolidation with

418 Lateral Drainage using Particle Image Velocimetry (PIV), KSCE J. Civ. Eng., doi:10.1007/s12205-017-

419 0707-6, 2017.

420 Kim, K., Kim, J., Kwak, T. Y. and Chung, C. K.: Logistic Regression Model for Sinkhole Susceptibility

421 due to Damaged Sewer Pipes, Nat. Hazards, 93(2), 765–785, doi:10.1007/s11069-018-3323-y, 2018.

422 Kristo, C., Rahardjo, H. and Satyanaga, A.: Effect of Variations in Rainfall Intensity on Slope Stability in

423 Singapore, Int. Soil Water Conserv. Res., 5(4), 258–264, doi:10.1016/j.iswcr.2017.07.001, 2017.

424 Kuwano, R., Horii, T., Yamauchi, K. and Kohashi, H.: Formation of Subsurface Cavity and Loosening due

425 to Defected Sewer Pipes, Japanese Geotech. J., 5(2), 349–361, 2010a.

426 Kuwano, R., Sato, M. and Sera, R.: Study on the Detection of Underground Cavity and Ground Loosening

427 for the Prevention of Ground Cave-in Accident, Japanese Geotech. J., 5(2), 349–361, 2010b.

428   Kwak, T., Kim, J., Lee, M. and Chung, C.-K.: Evaluation of the Factors Contributing to the Occurrence of

429   Ground Cave-ins and Subsidence Induced by a Damaged Sewer Pipeline, in Civil Engineering Conference

430   in the Asian Region (CECAR 7), Hawaii, USA., 2016.

431   Kwak, T. Y., Woo, S. I., Kim, J. and Chung, C. K.: Model Test Assessment of the Generation of

432   Underground Cavities and Ground Cave-ins by Damaged Sewer Pipes, Soils Found., 59(3), 586–600,

433   doi:10.1016/j.sandf.2018.12.011, 2019.

434   Martinotti, M. E., Pisano, L., Marchesini, I., Rossi, M., Peruccacci, S., Brunetti, M. T., Melillo, M.,

435   Amoruso, G., Loiacono, P., Vennari, C., Vessia, G., Trabace, M., Parise, M. and Guzzetti, F.: Landslides,

436   Floods and Sinkholes in a Karst Environment: The 1-6 September 2014 Gargano event, southern Italy, Nat.

437   Hazards Earth Syst. Sci., 17(3), 467–480, doi:10.5194/nhess-17-467-2017, 2017.

438   Ministry of Environment of Korea: Technical Standard for Construction of Sewer Pipes, 2010.

439   Mukunoki, T., Kumano, N. and Otani, J.: Image Analysis of Soil Failure on Defective Underground Pipe

440   due to Cyclic Water Supply and Drainage using X-ray CT, Front. Struct. Civ. Eng., 6(2), 85–100,

441   doi:10.1007/s11709-012-0159-5, 2012.

442   Nadarajah, S. and Choi, D.: Maximum Daily Rainfall in South Korea, J. Earth Syst. Sci., 116(4), 311–320,

443   doi:10.1007/s12040-007-0028-0, 2007.

444   National Diaster Management Institute of Korea: Possibility of Manhole Cap Removal by Heavy Rainfall,

445   Minist. Secur. Public Adm. Korea Press Releases, 1–6, 2014.

446   Oosthuizen, A. C. and Richardson, S.: Sinkholes and subsidence in South Africa. [online] Available from:

447   http://www.geohazard.org.za/images/docs/subsection_downloads/Sinkholes.pdf, 2011.

448   Parise, M.: A procedure for evaluating the susceptibility to natural and anthropogenic sinkholes, Georisk, 9

449   (4), 272-285, doi:10.1080/17499518.2015.1045002, 2015.

450   Parise, M., Pisano, L. and Vennari, C.: Sinkhole clusters after heavy rainstorms, Journal of Cave and Karst

451   Studies, 80 (1), 28-38, doi: 10.4311/2017ES0105, 2018.

452   Parise, M.: Sinkholes. In: White W.B., Culver D.C. & Pipan T. (Eds.), Encyclopedia of Caves. Academic

453   Press, Elsevier, 3rd edition, ISBN 978-0-12-814124-3, 934-942, 2019.

454   Peruccacci, S., Brunetti, M. T., Luciani, S., Vennari, C. and Guzzetti, F.: Lithological and seasonal control

455   on rainfall thresholds for the possible initiation of landslides in central Italy, Geomorphology, 139–140,

456   79–90, 2012.

457   Rahardjo, H., Kim, Y. and Satyanaga, A.: Role of Unsaturated Soil Mechanics in Geotechnical

458   Engineering, Int. J. Geo-Engineering, 10(1), 1–23, doi:10.1186/s40703-019-0104-8, 2019.

459   Rogers, C. J.: Sewer Deterioration Studies: The Background to the Structural Assessment Procedure in the

460   Sewerage Rehabilitation Manual., 1986.

461   Rossi, M., Peruccacci, S., Brunetti, M. T., Marchesini, I., Luciani, S., Ardizzone, F., Balducci, V., Bianchi,

462   C., Cardinali, M., Fiorucci, F., Mondini, A. C., Reichenbach, P., Salvati, P., Santangelo, M., Bartolini, D.,

463   Gariano, S. L., Palladino, M., Vessia, G., Viero, A., Antronico, L., Borselli, L., Deganutti, A. M., Iovine,

464   G., Luino, F., Parise, M., Polemio, M. and Guzzetti, F.: SANF: a national warning system for rainfall-

465   induced landslides in Italy, in: Proceedings of the 11th International Conference and 2nd North American

466   symposium on landslides, Banff, Alberta, Canada, 3–8 June, 2012.

467   Sato, M. and Kuwano, R.: Influence of Location of Subsurface Structures on Development of Underground

468   Cavities induced by Internal Erosion, Soils Found., 55(4), 829–840, doi:10.1016/j.sandf.2015.06.014, 2015.

469   Tang, Y., Zhu, D. Z. and Chan, D. H.: Experimental Study on Submerged Sand Erosion through a Slot on a

470   Defective Pipe, J. Hydraul. Eng., 143(9), 1–14, doi:10.1061/(ASCE)HY.1943-7900.0001326, 2017.

471   Van Den Eeckhaut, M., Poesen, J., Dusar, M., Martens, V. and Duchateau, P.: Sinkhole formation above

472   underground limestone quarries: A case study in South Limburg (Belgium), Geomorphology, 91(1–2), 19–

473   37, doi:10.1016/j.geomorph.2007.01.016, 2007.

474   Vessia, G., Parise, M., Brunetti, M.T., Peruccacci, S., Rossi, M., Vennari, C. and Guzzetti, F.: Automated

475   reconstruction of rainfall events responsible for shallow landslides. Natural Hazards and Earth System

476   Sciences, 14, 2399- 2408, 2014.

477   Waltham, T., Bell, F. and Culshaw, M.: Sinkholes and Subsidence, Springer, Chichester, 2005.

478   White, D. J. and Take, W. A.: GeoPIV: Particle Image Velocimetry (PIV) Software for Use in

479   Geotechnical Testing, Cambridge Univ. Eng. Dep. Tech. Rep., 322(October), 15, 2002.

480   White, D. J., Take, W. A. and Bolton, M. D.: Soil Deformation Measurement using Particle Image

481   Velocimetry (PIV) and Photogrammetry, Geothechnique, 53(7), 619–631, doi:10.1680/geot.2003.53.7.619,

482   2003.

483   Wi, S., Valdés, J. B., Steinschneider, S. and Kim, T. W.: Non-stationary Frequency Analysis of Extreme

484   Precipitation in South Korea using Peaks-over-threshold and Annual Maxima, Stoch. Environ. Res. Risk

485   Assess., 30(2), 583–606, doi:10.1007/s00477-015-1180-8, 2016.

486   Yokota, T., Fukatani, W. and Miyamoto, T.: The present situation of the road cave in sinkholes caused by

487   sewer systems., 2012.
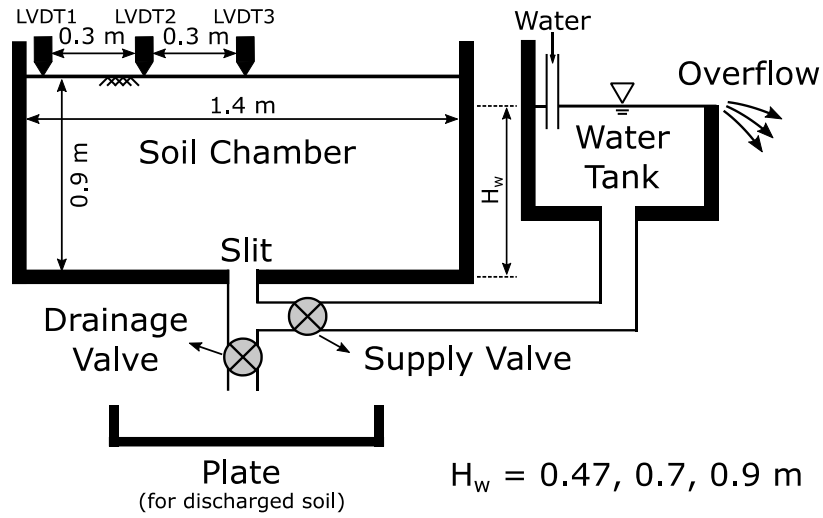
488
489 **Figure 1: Schematic of the model test device.**

490

491
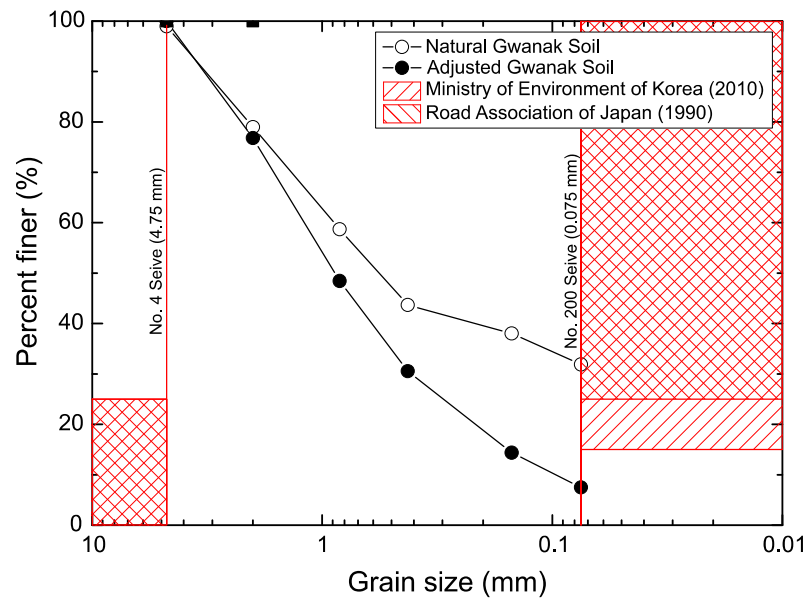
492 **Figure 2: Grain distribution of the natural Gwanak soil and the Gwanak soil adjusted as per the requirements**
493 **for backfill materials in South Korea (Ministry of Environment of Korea, 2010) and Japan (Japan Road**
494 **Association, 1990).**

495

496
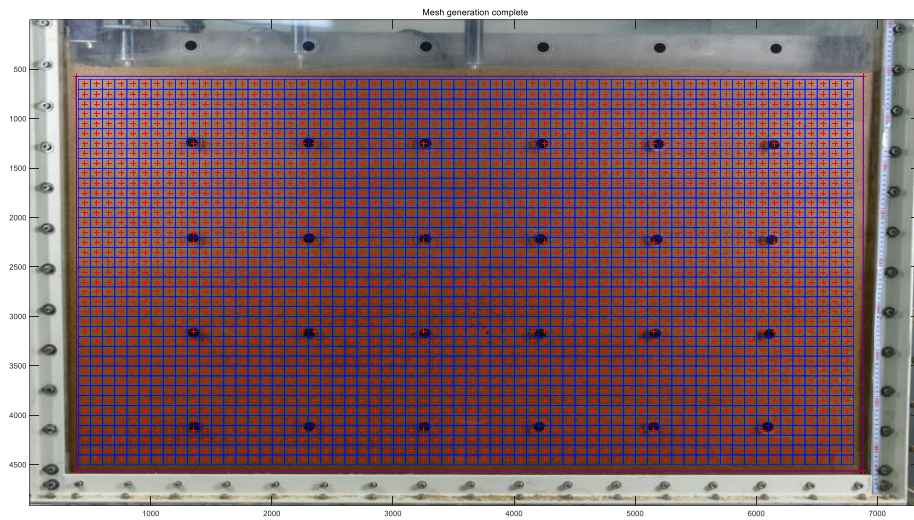
497   **Figure 3: Selected pixel subsets and center points for digital image analysis.**

498
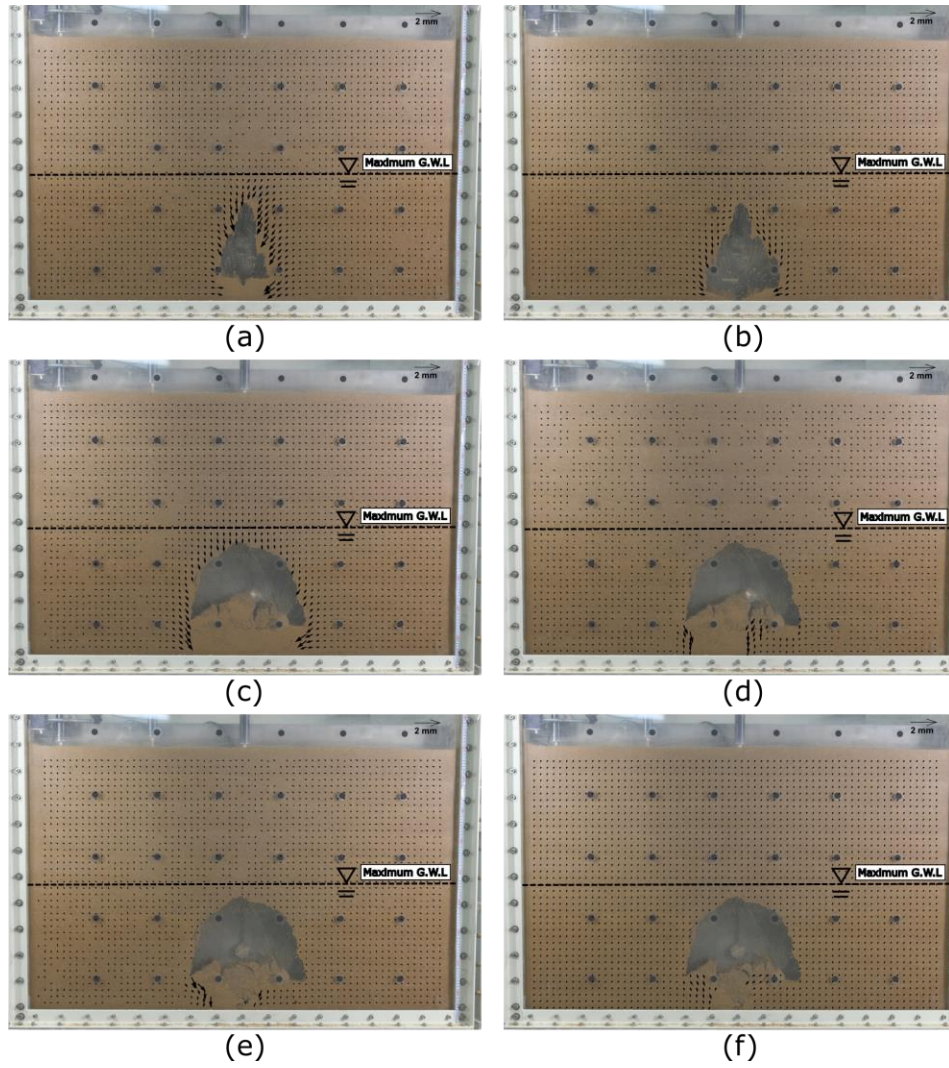
Figure 4: Displacement increment vectors inside the model ground for Test 1 during the water drainage stage: (a) 0–30 s, (b) 30–60 s, (c) 60–90 s, (d) 90–120 s, (e) 120–150 s, and (f) 150–180 s.
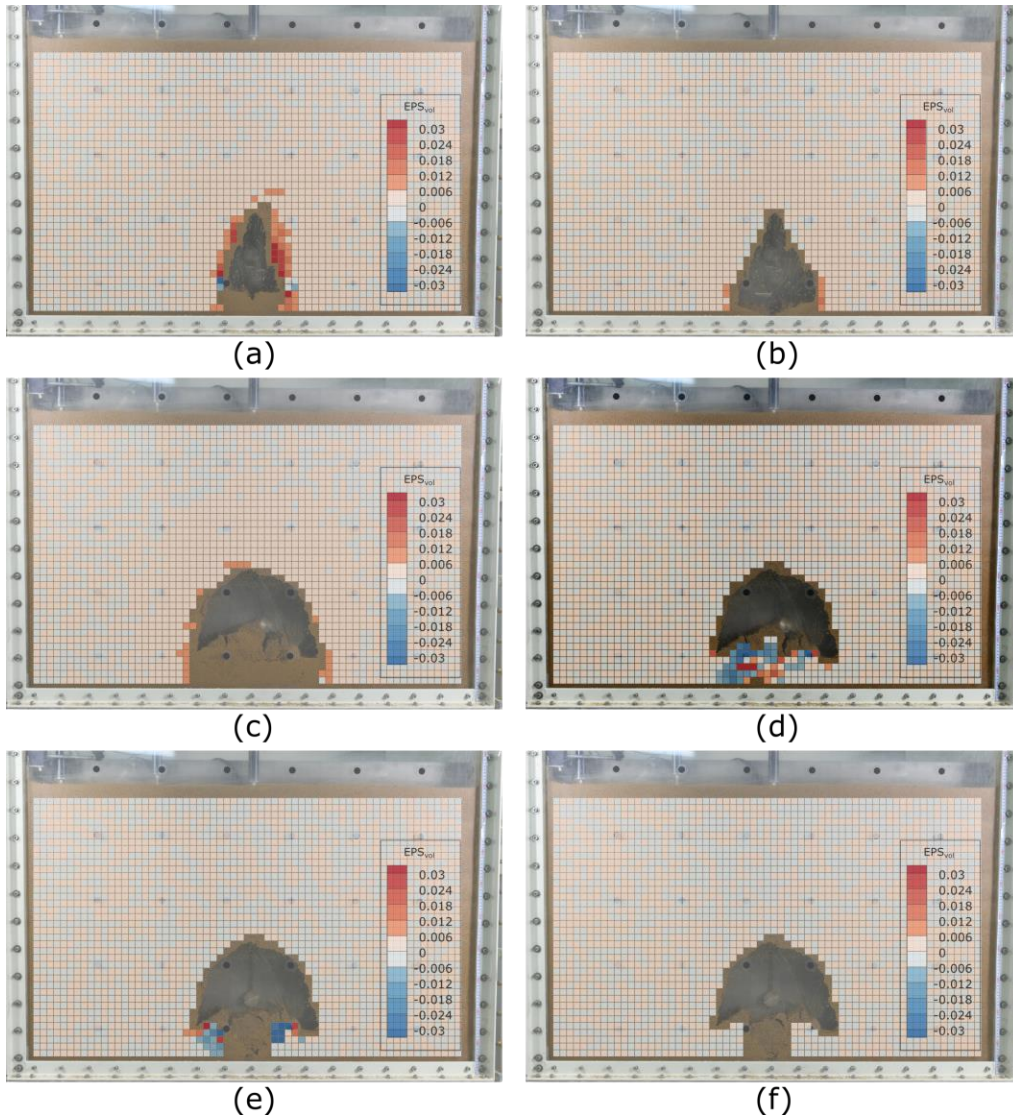
Figure 5: Volumetric strain inside the model ground for Test 1 during the water drainage stage: (a) 0–30 s (b) 30–60 s, (c) 60–90 s, (d) 90–120 s, (e) 120–150 s, and (f) 150–180 s.

507
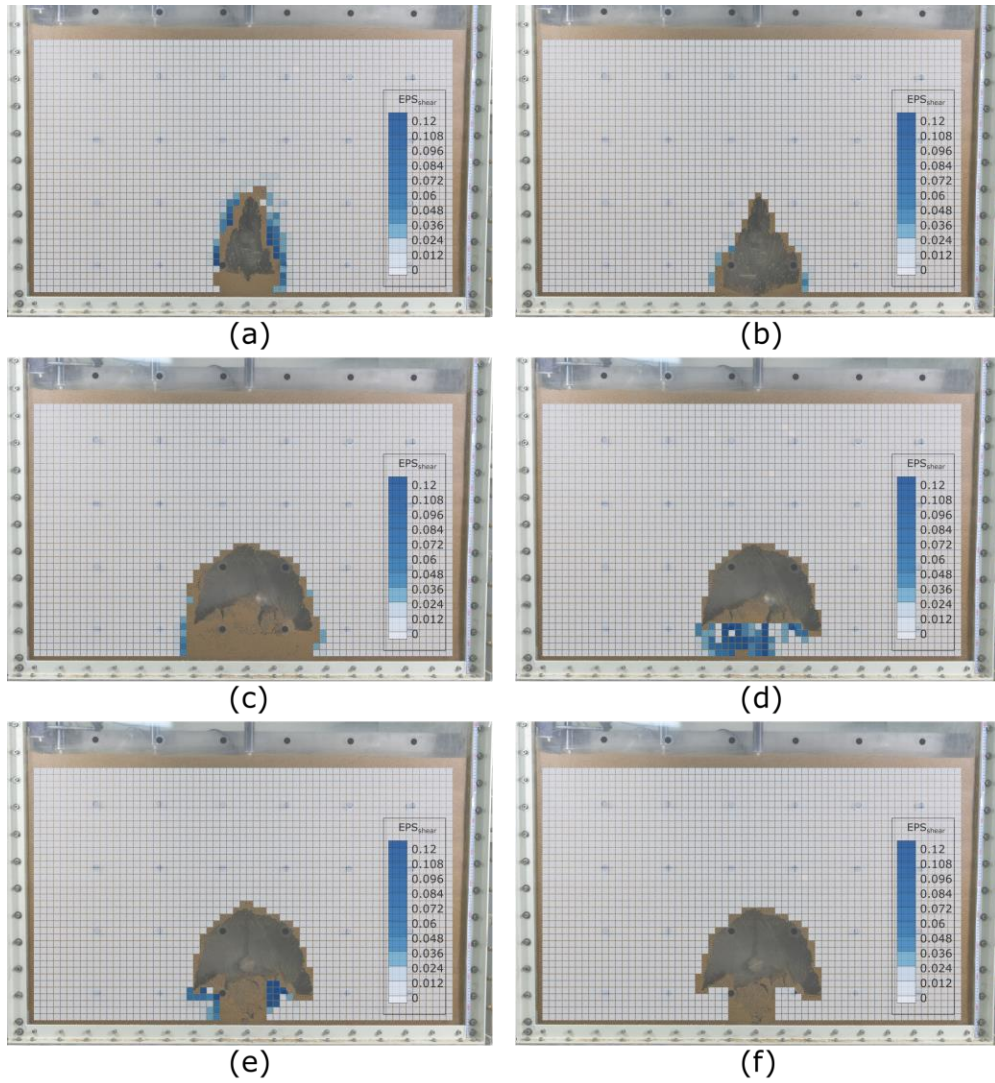
508 **Figure 6: Shear strain inside the model ground for Test 1 during the water drainage stage: (a) 0–30 s, (b) 30–60**
509 **s, (c) 60–90 s, (d) 90–120 s, (e) 120–150 s, and (f) 150–180 s.**

510

511
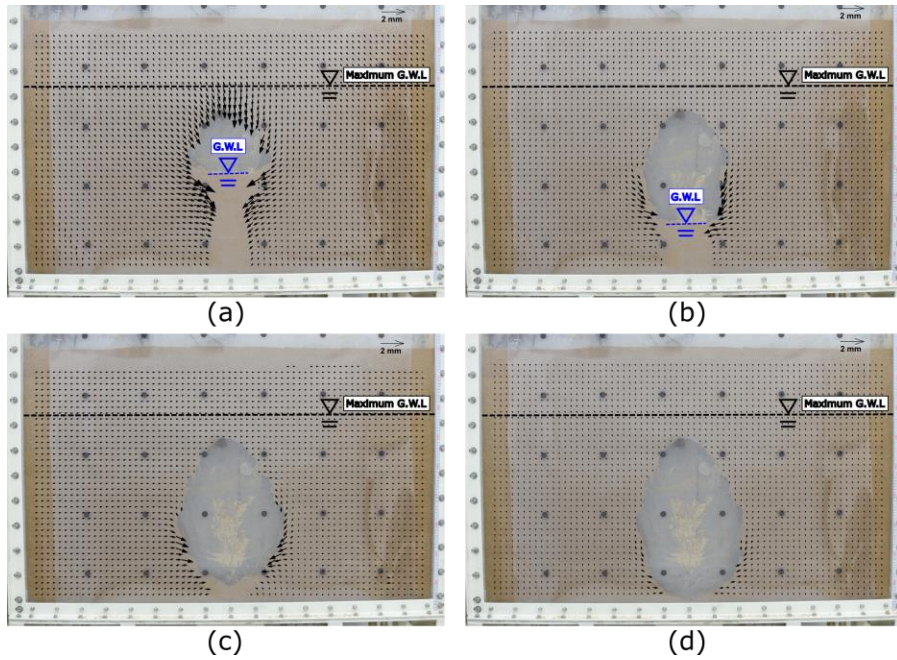
Figure 7: Displacement increment vectors inside the model ground for Test 2 during the water drainage stage: (a) 0–30 s, (b) 30–60 s, (c) 60–90 s, and (d) 90–120 s.

514

515
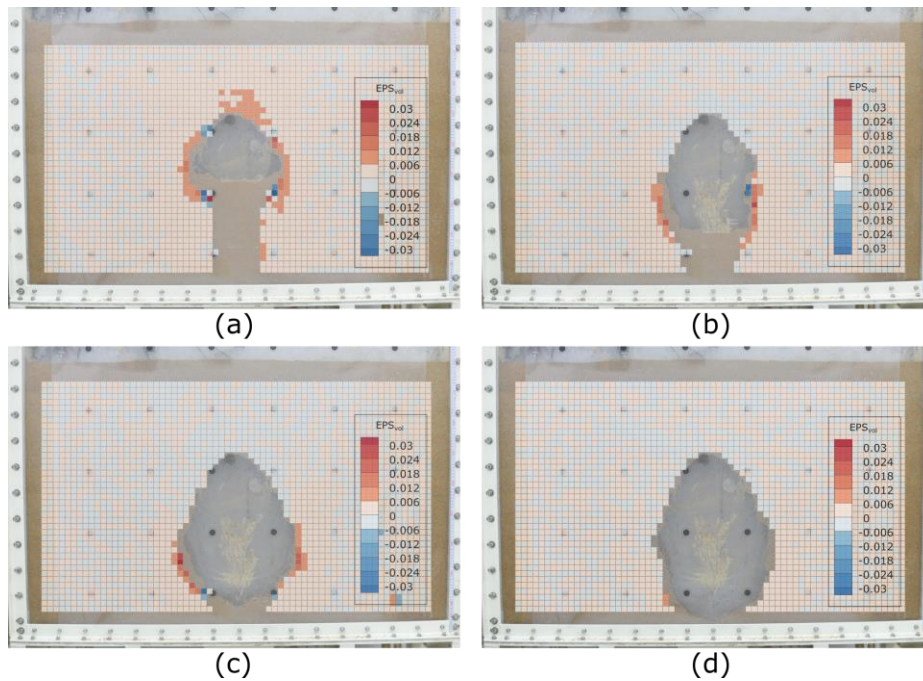
Figure 8: Volumetric strain inside the model ground for Test 2 during the water drainage stage: (a) 0–30 s, (b) 30–60 s, (c) 60–90 s, and (d) 90–120 s.

518

519
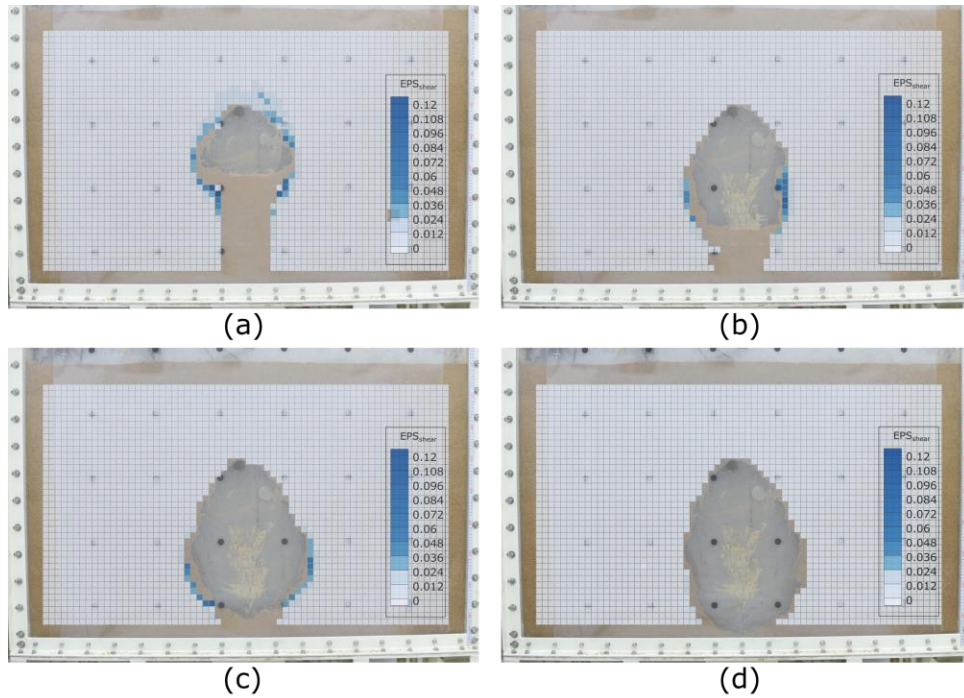
520 **Figure 9: Shear strain inside the model ground for Test 2 during the water drainage stage: (a) 0–30 s, (b) 30–60**
521 **s, (c) 60–90 s, and (d) 90–120 s.**

522

523
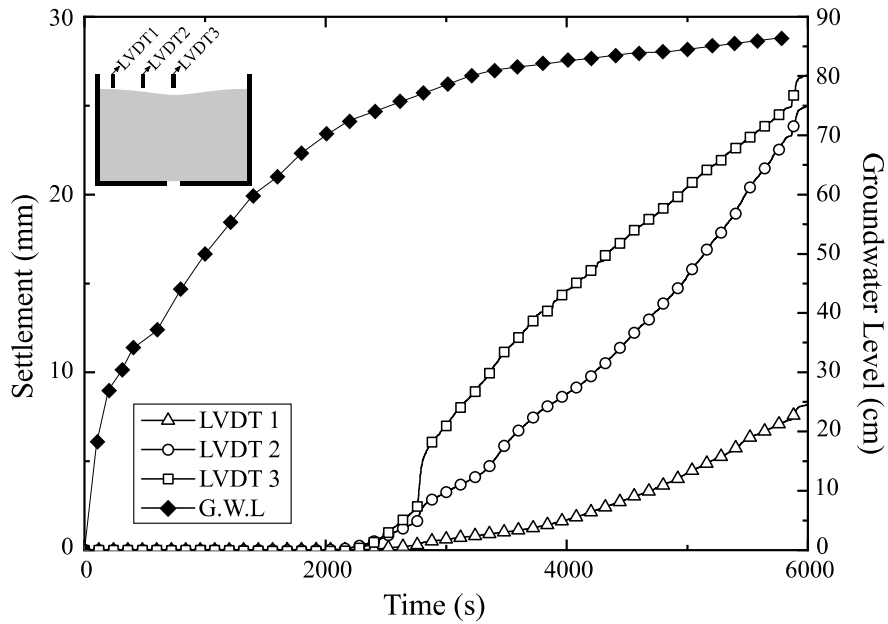
524 **Figure 10: LVDT measurement during the water supply stage (Test 3).**

525

(a)

(b)

(c)

(d)
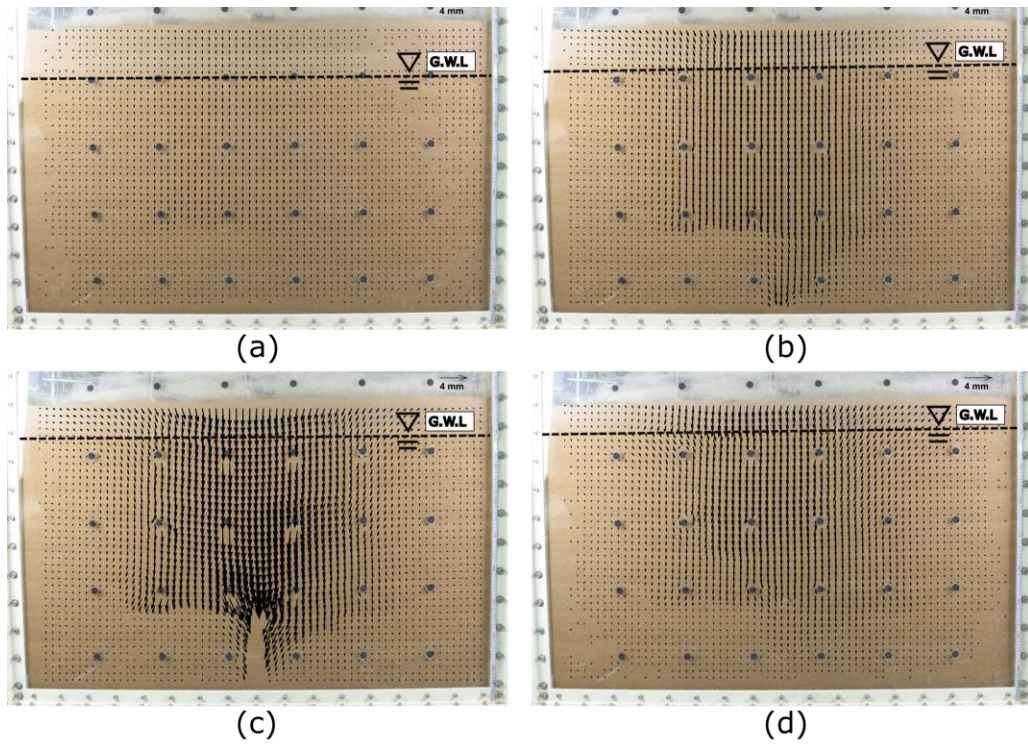
526

527 **Figure 11: Displacement increment vectors inside the model ground for Test 3 during the water supply stage: (a)**
528 **2000–2400 s, (b) 2400–2800 s, (c) 2800–3200 s, and (d) 3200–3600 s.**

529

530
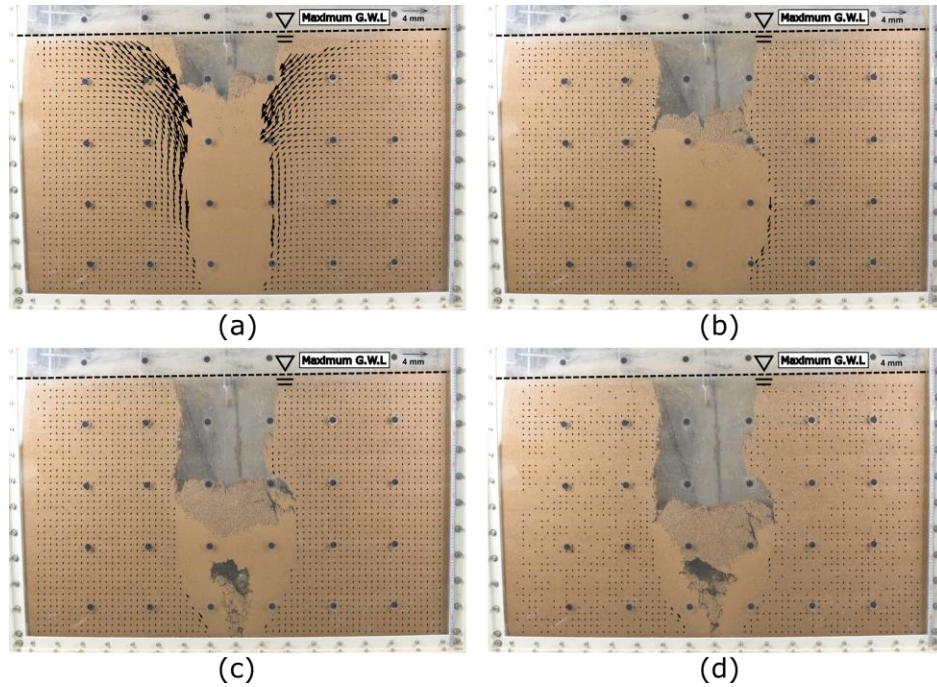
531   **Figure 12: Displacement increment vectors inside the model ground for Test 3 during the water drainage stage:**
532   **(a) 0–30 s, (b) 30–60 s, (c) 60–90 s, and (d) 90–120 s.**

533
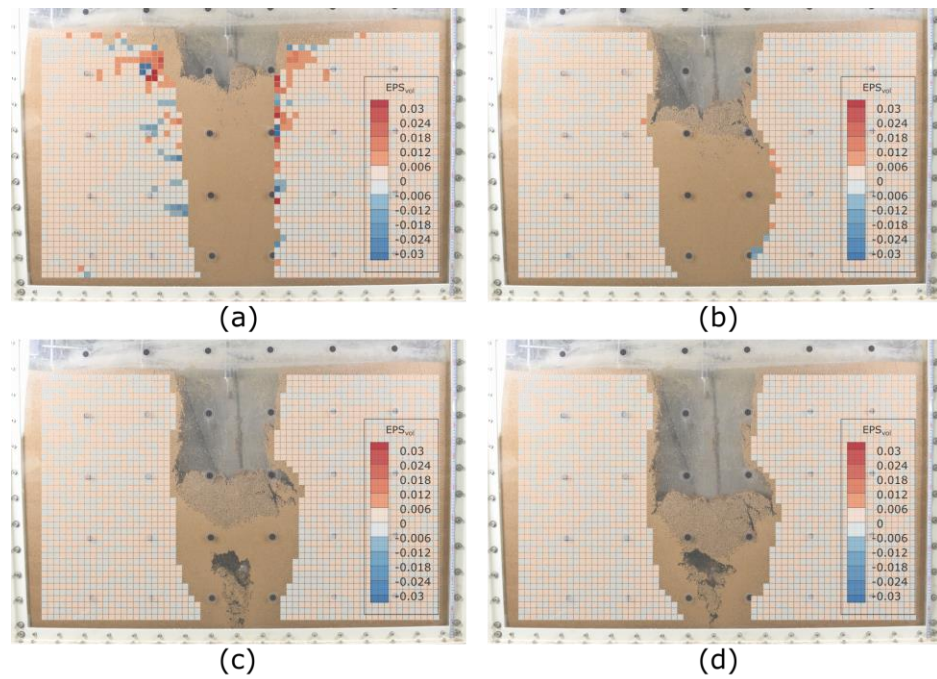
534   **Figure 13: Volumetric strain inside the model ground for Test 3 during the water drainage stage: (a) 0–30 s, (b)**
535   **30–60 s, (c) 60–90 s, and (d) 90–120 s.**

536

537
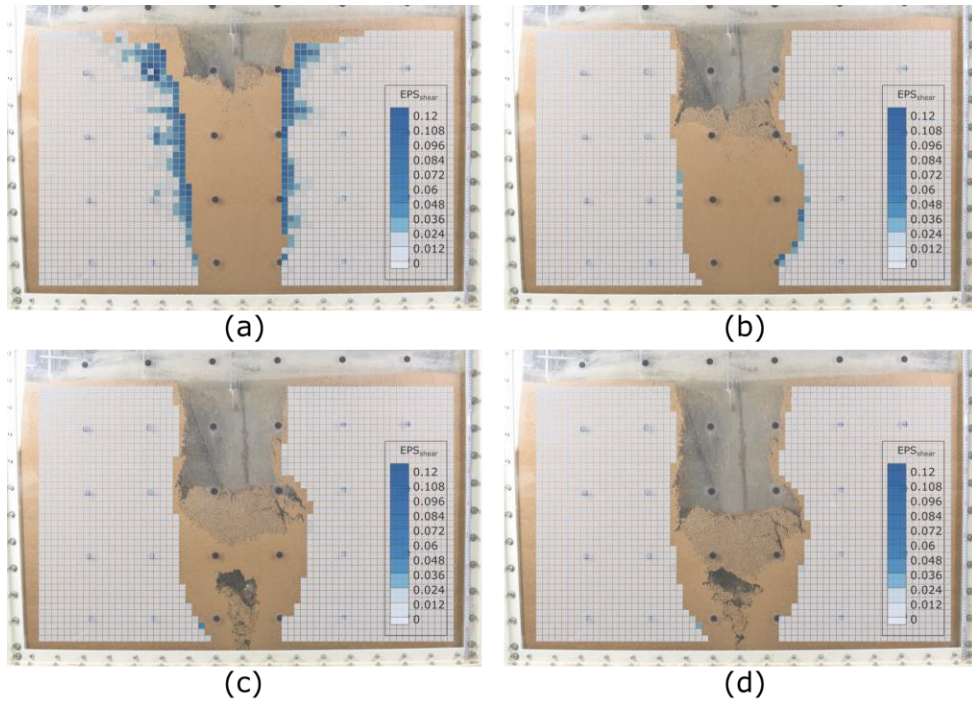
Figure 14: Shear strain inside the model ground for Test 3 during the water drainage stage: (a) 0–30 s, (b) 30–60 s, (c) 60–90 s, and (d) 90–120 s.

540

541
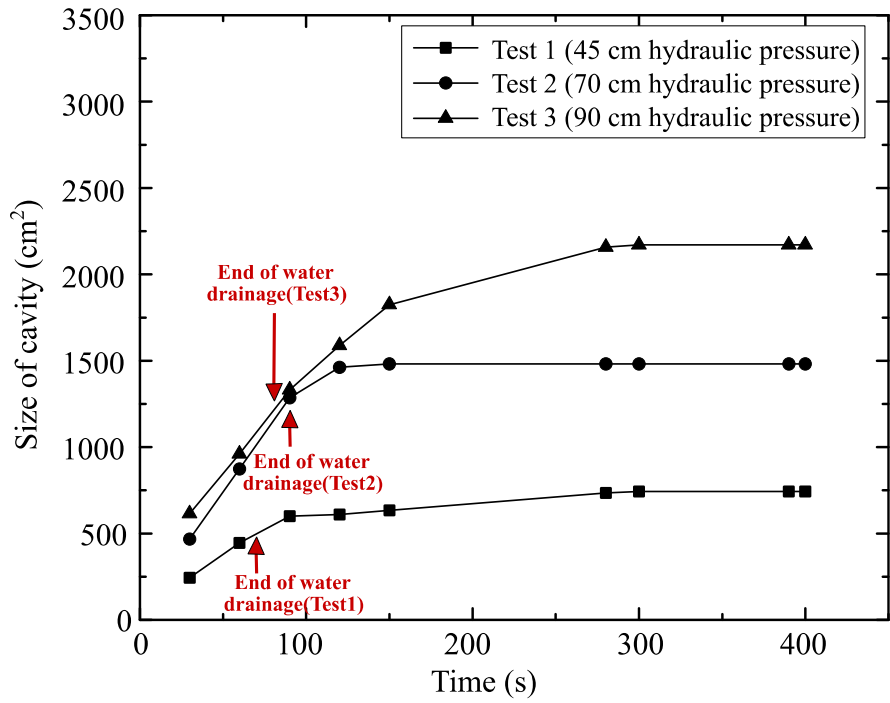
Figure 15: Sizes of cavities developed during the water drainage stage in each test.

543 **Table 1: Relation between rainfall intensity and hydraulic head applied to sewer pipes**
544 **(National Diaster Management Institute of Korea, 2014).**

Rainfall intensity	Hydraulic head
20 mm/h	33 cm
30 mm/h	40 cm
40 mm/h	47 cm
50 mm/h	70 cm

545

546 **Table 2: Properties of adjusted Gwanak soil.**

Description		Adjusted Gwanak soil (Fine content 7.5 %)
Classification in USCS (Unified Soil Classification System)		SW-SM
Specific gravity G_S		2.62
Mean grain size D_{50} (mm)		1.013
Coefficient of curvature C_C		1.24
Coefficient of uniformity C_U		12.4
Standard maximum dry unit weight* $\gamma_{d,max}$ (kN/m^3)		18.5
e_{max} / e_{min}		0.96 / 0.39
Void ratio		0.51
Optimum water content* (%)		11.4
Strength parameter**	Saturation S 100 %	Cohesion c (kPa)	3.9
		Friction angle ϕ (°)	36.3
	Saturation S 44.2 %	Cohesion c (kPa)	15.8
		Friction angle ϕ (°)	38.3
Saturated permeability coefficient k_{sat} (cm/s)		1.45 x 10^{-4}

547 * Estimated from the standard compaction tests
548 ** Estimated from the direct shear tests; S = 44.2 % corresponds to w_{opt} obtained from the standard compaction tests

549 **Table 3: Model test conditions used in this study.**

Test No.	Soil type	Slit size	Degree of compaction D_C (Relative density D_R)	Burial depth	Maximum groundwater level
#1					47 cm
#2	Adjusted Gwanak soil	2 cm	93 % (78 %)	90 cm	70 cm
#3					90 cm

550

551 **Table 4: Comparative studies of the model tests.**

Test	Test 1 (47 cm G.W.L)	Test 2 (70 cm G.W.L)	Test 3 (90 cm G.W.L)
Percentage of the weight of the discharged soil in the total initial weight of the model ground	6.4 %	12.9 %	18.3 %
Percentage of the volume of the eroded zone(cavity or sinkhole) in the total initial volume of the model ground	5.9 %	12.5 %	18.2 %
Ratio of average cavity width[*] to slit width	11.5 (22.9 / 2 cm)	13.1 (26.2 / 2 cm)	16.4 (32.8 / 2 cm)
Average density change in the loosening zone	−3.1 kN/m3	−3.7 kN/m3	−2.9 kN/m3

552 * Calculated by dividing the cavity size (via Image J software) by the height of cavity.